Electronic Supplementary Material (ESI) for Inorganic Chemistry Frontiers.

Modulation of Halogens in Organic Manganese Halides for High-resolution and Large-area Flexible X-ray Imaging

Ying Sun,[a] Qian Ma,[b] Dongheng Zhao,[b] Pan Gao,[a] Qi Wang,[a] Zeyu Guo,[a] and Xiaomei Jiang[a*]

[a]School of Preventive Medicine Sciences (Institute of Radiation Medicine), Shandong First Medical University & Shandong Academy of Medical Sciences, No. 6699 Qingdao Road, Jinan n 250117, People's Republic of China

[b]School of Material Science and Engineering, University of Jinan, No.336 Nanxinzhuang West Road, Jinan 250022, People's Republic of China.

***Corresponding authors.**

E-mail addresses: jiangxiaomei@sdfmu.edu.cn

Table S1. Crystallographic data and refinement details for $(C_6H_8N)_2MnX_4$ (X=Cl, Br, I).

Empirical	$(C_6H_8N)_2MnCl_4$	$(C_6H_8N)_2MnBr_4$	$(C_6H_8N)_2MnI_4$
Formula Weight/g·mol^{-1}	385.01	562.85	750.81
Crystal System	monoclinic	monoclinic	orthorhombic
Space Group	I2/a	C2/c	Pbca
Unit Cell Dimensions	a=16.0523(11) Å b=8.4560(4) Å c=26.4946(19) Å α=γ=90° β=104.499(7)°	a= 27.928(6) Å b= 8.7713(17) Å c= 16.385(3) Å α=γ=90° β=110.162(7) °	a=8.7700(10) Å b= 15.195(2) Å c= 31.508(4) Å α=γ=β=90°
Volume/Å^3	3481.8(4) Å^3	3767.8(13) Å^3	4198.76(9)
ρ_{calc}/g·cm^{-3}	1.469	1.98435	2.375
Z	8	8	8
Index Ranges	-14 ≤ h ≤ 19, -10 ≤ k ≤ 8, -31 ≤ l ≤ 31	-33 ≤ h ≤ 33, -10 ≤ k ≤ 10, -19 ≤ l ≤ 19	-10 ≤ h ≤ 10, -18 ≤ k ≤ 18, -37 ≤ l ≤ 37
Radiation	MoKα (λ = 0.71073)	MoKα (λ = 0.71073)	MoKα (λ = 0.71073)
Reflections Collected	8063	27467	59278
Independent Reflections	3051 [R_{int} = 0.0216, R_{sigma} = 0.0270]	3319 [R_{int} = 0.1047, R_{sigma} = 0.0495]	3698 [R_{int} = 0.0619, R_{sigma} = 0.0219]
Data/Restraints /Parameters	3051/33/178	3319/0/182	3698/0/179
Goodness-of-Fit	1.065	1.015	1.060
Final R Indices [I > 2σ(I)]	R_1 = 0.0328, wR_2 = 0.0784	R_1 = 0.0349, wR_2 = 0.0584	R_1 = 0.0244, wR_2 = 0.0433
R Indices [all data]	R_1 = 0.0431, wR_2 = 0.0836	R_1 = 0.0691, wR_2 = 0.0657	R_1 = 0.0326, wR_2 = 0.0459
Largest Diff. Peak and Hole/ e Å^{-3}	0.31/-0.19	0.40/-0.39	0.60/-0.67
2Theta Range (Data Collection)/°	6.66 to 49.992	4.898 to 49.998	5.172 to 49.996
CCDC Number	2381212	2270667	2381207

Table S2. Selected bond lengths and angles for $(C_6H_8N)_2MnX_4$ (X=Cl, Br, I).

Atom	Atom	Length/Å	Atom	Atom	Atom	Angle/°
			$(C_6H_8N)_2MnCl_4$			
Mn1	Cl2	2.3421	Cl2	Mn1	Cl1	112.859
Mn1	Cl1	2.3428	Cl2	Mn1	Cl3	111.459
Mn1	Cl3	2.3639	Cl2	Mn1	Cl4	108.223
Mn1	Cl4	2.3739	Cl1	Mn1	Cl3	108.377
N1	C5	1.339	Cl1	Mn1	Cl4	106.062
N1	C1	1.326	Cl3	Mn1	Cl4	109.697
			$(C_6H_8N)_2MnBr_4$			
Mn1	Br2	2.4808	Br2	Mn1	Br1	112.684
Mn1	Br1	2.4896	Br2	Mn1	Br3	108.427
Mn1	Br3	2.4993	Br1	Mn1	Br3	111.061
Mn1	Br4	2.5193	Br2	Mn1	Br4	105.96
N2	C5	1.342	Br3	Mn1	Br4	110.06
N2	C1	1.337	Br1	Mn1	Br4	108.52
			$(C_6H_8N)_2MnI_4$			
I3	Mn1	2.7199	I4	Mn1	I3	108.12
I4	Mn1	2.6839	I4	Mn1	I2	112.19
I2	Mn1	2.6864	I4	Mn1	I1	108.74
I1	Mn1	2.7171	I2	Mn1	I3	112.24
N2	C11	1.356	I2	Mn1	I1	105.50
N2	C7	1.343	I1	Mn1	I3	109.99

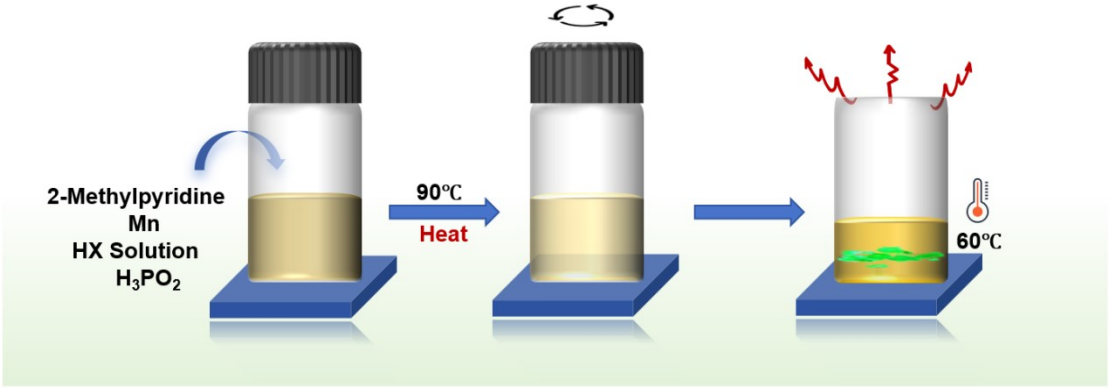

Fig. S1. Schematic diagram of $(C_6H_8N)_2MnX_4$ (X=Cl, Br, I) single crystals being grown by the slow solution evaporation method.

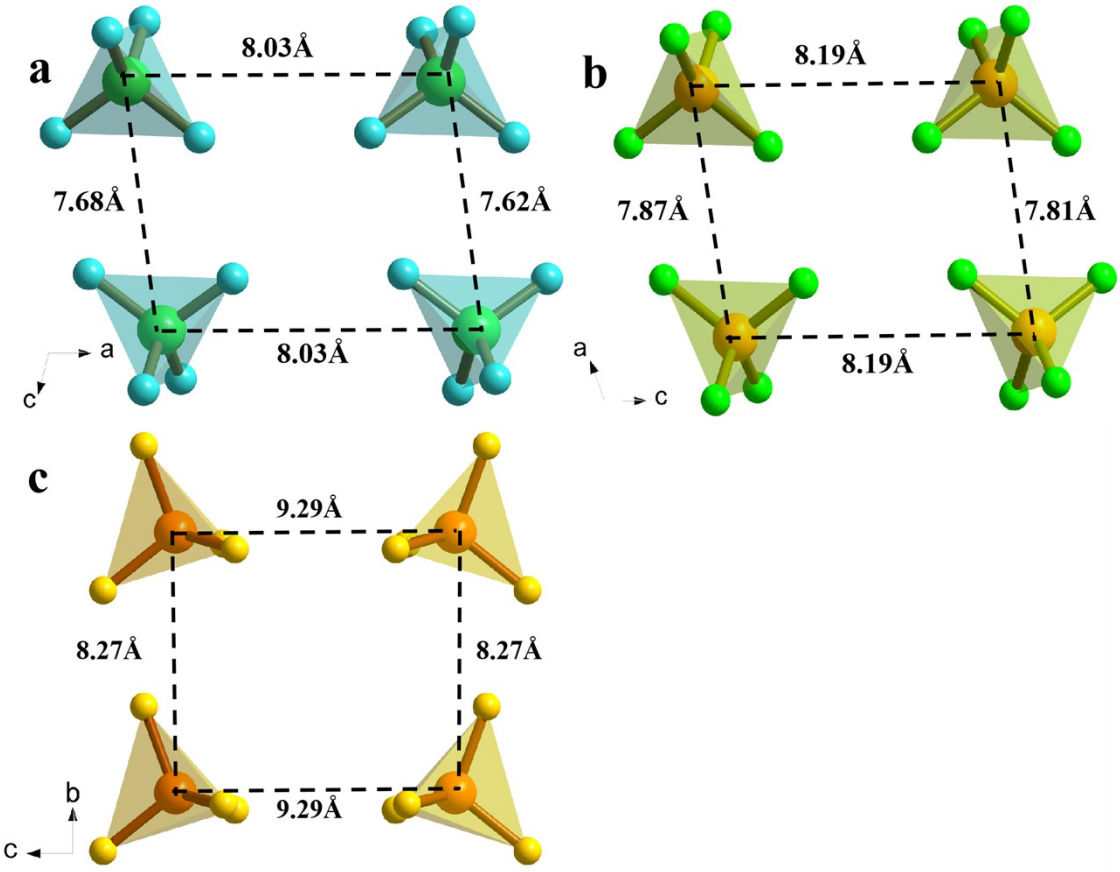

Fig. S2. The structure of $[MnBr_4]^{2-}$s showing the Mn-Mn distance for (a) $(C_6H_8N)_2MnCl_4$, (b) $(C_6H_8N)_2MnBr_4$ and (c) $(C_6H_8N)_2MnI_4$.

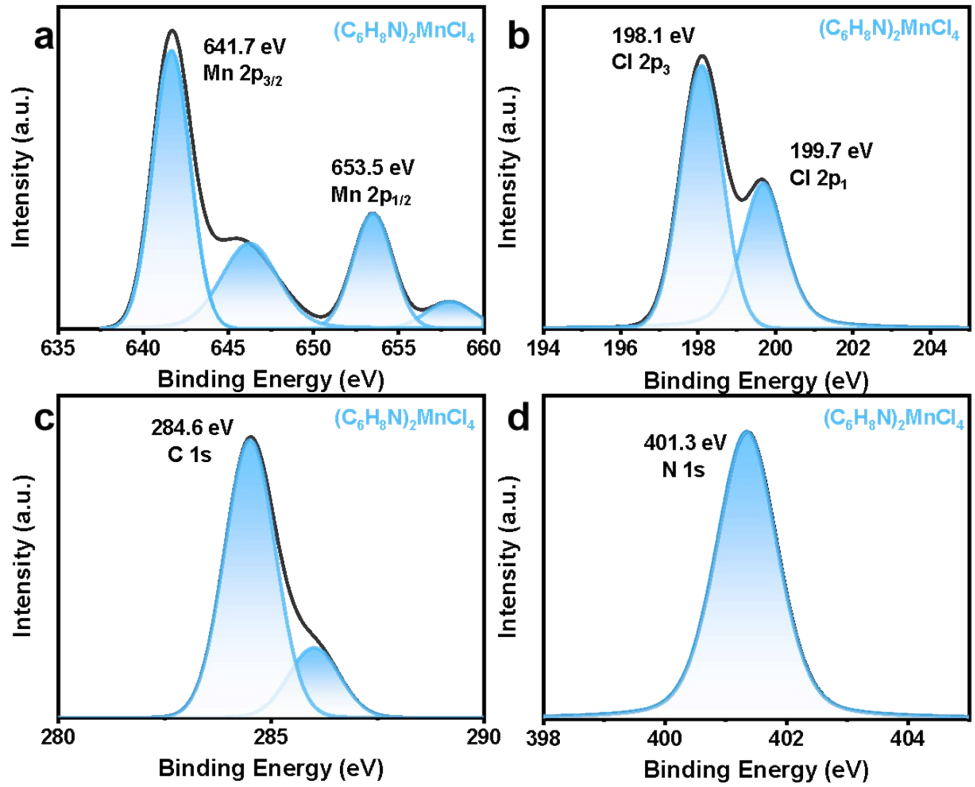

Fig. S3. High-resolution XPS spectra of (a) Mn 2p, (b) Cl 2p, (c) C 1s and (d) N 1s of $(C_6H_8N)_2MnCl_4$.

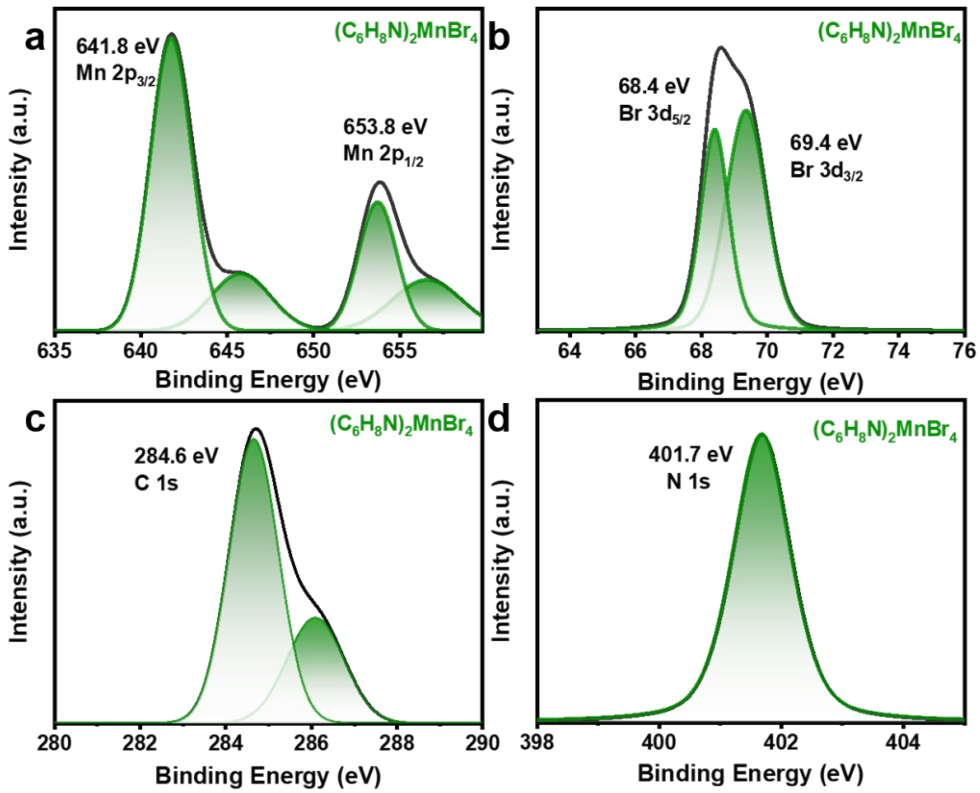

Fig. S4. High-resolution XPS spectra of (a) Mn 2p, (b) Br 3d, (c) C 1s and (d) N 1s of $(C_6H_8N)_2MnBr_4$.

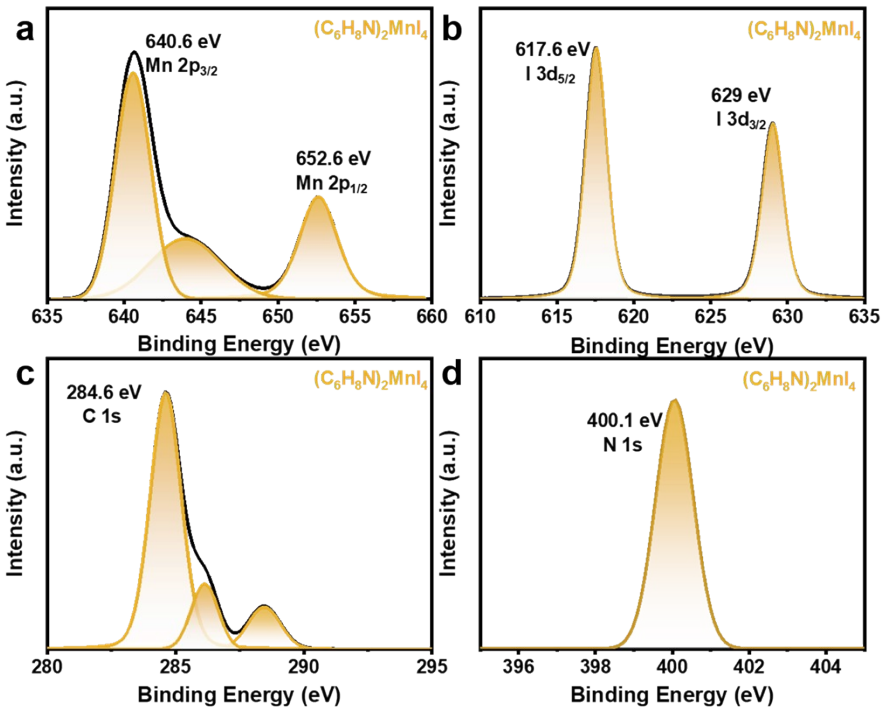

Fig. S5. High-resolution XPS spectra of (a) Mn 2p, (b) I 3d, (c) C 1s and (d) N 1s of $(C_6H_8N)_2MnI_4$.

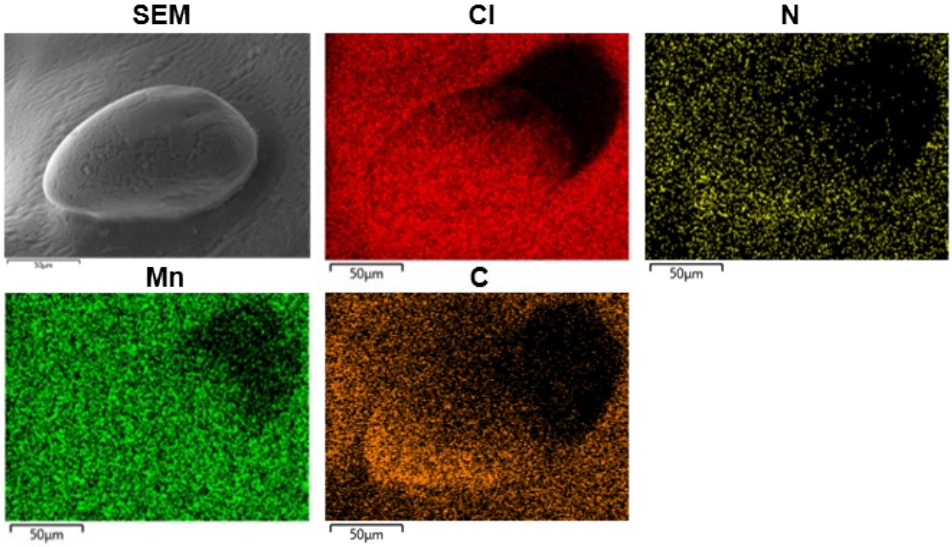

Fig. S6. Scanning electron microscopy (SEM) image and energy-dispersive spectroscopy (EDS) elemental mapping images of C, N, Mn and Cl of $(C_6H_8N)_2MnCl_4$.

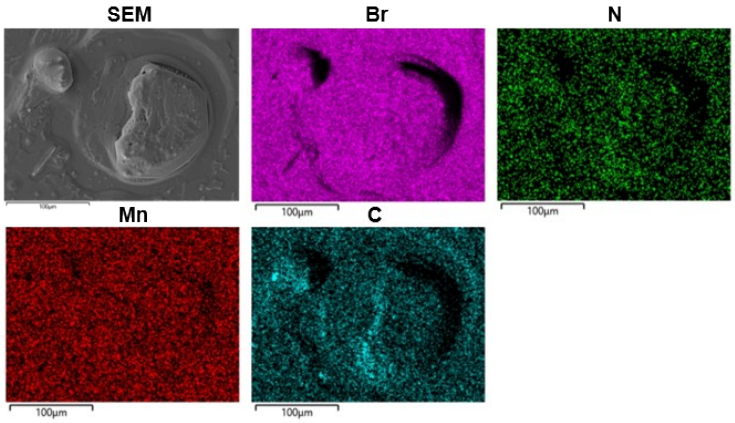

Fig. S7. Scanning electron microscopy (SEM) image and energy-dispersive spectroscopy (EDS) elemental mapping images of C, N, Mn and Br of $(C_6H_8N)_2MnBr_4$.

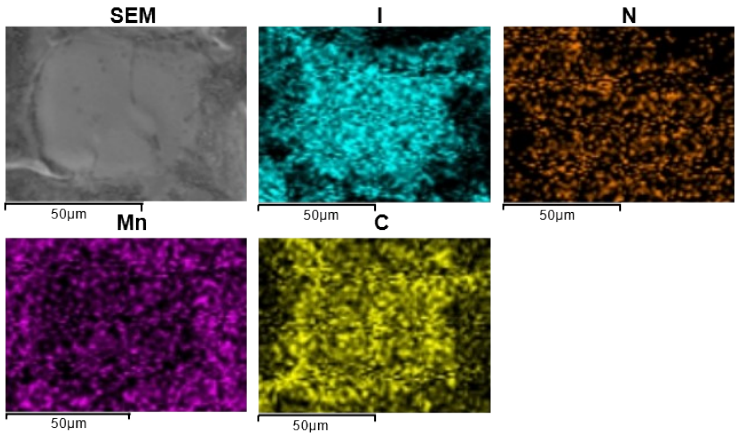

Fig. S8. Scanning electron microscopy (SEM) image and energy-dispersive spectroscopy (EDS) elemental mapping images of C, N, Mn and I of $(C_6H_8N)_2MnI_4$.

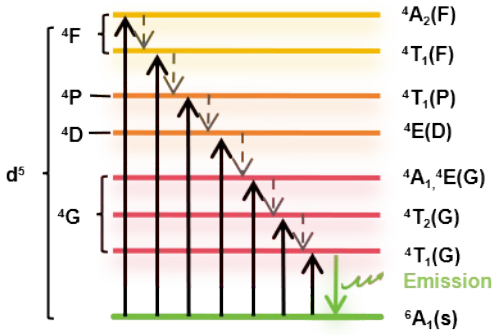

Fig. S9. Schematic diagram of the PL mechanism of $(C_6H_8N)_2MnX_4$ (X=Cl, Br, I).

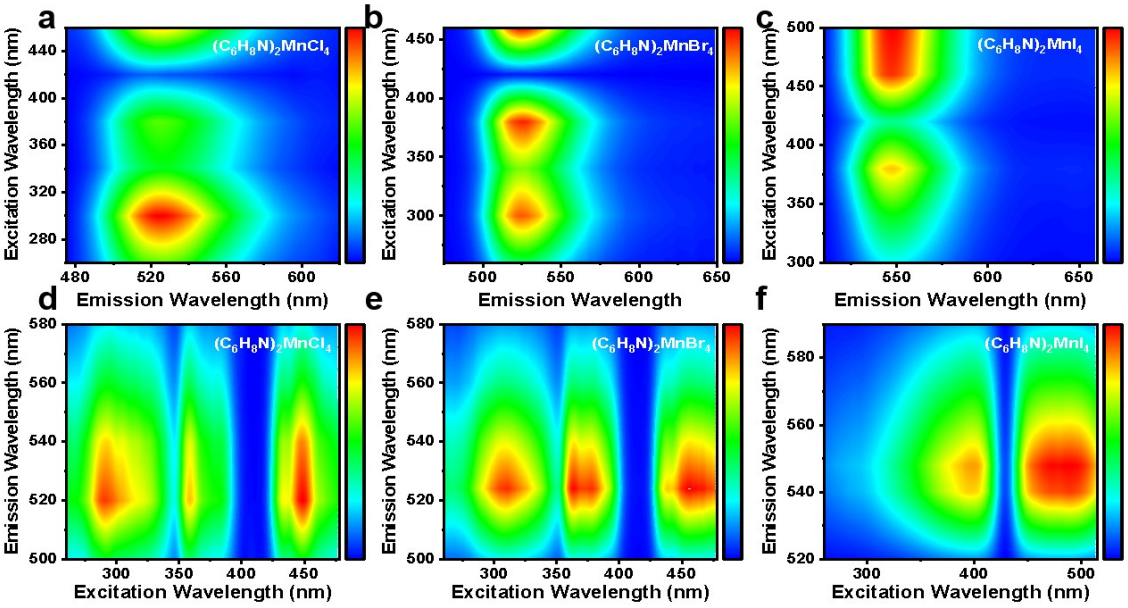

Fig. S10. PL spectra excited at different wavelengths of (a) $(C_6H_8N)_2MnCl_4$, (b) $(C_6H_8N)_2MnBr_4$ and (c) $(C_6H_8N)_2MnI_4$. PLE spectra at different emission wavelengths of (d) $(C_6H_8N)_2MnCl_4$, (e) $(C_6H_8N)_2MnBr_4$ and (f) $(C_6H_8N)_2MnI_4$.

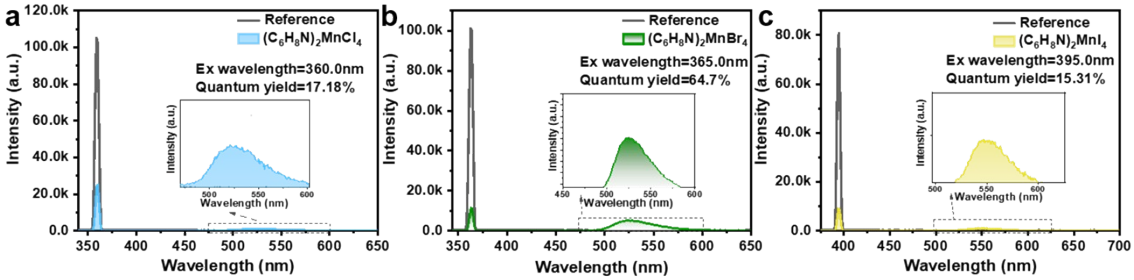

Fig. S11. Photoluminescence quantum yield (PLQY) of (a) $(C_6H_8N)_2MnCl_4$, (b) $(C_6H_8N)_2MnBr_4$ and (c) $(C_6H_8N)_2MnI_4$.

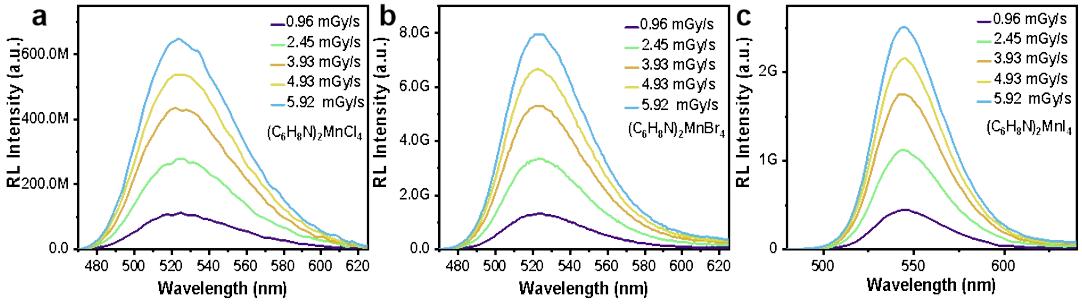

Fig. S12. RL spectra of (a) $(C_6H_8N)_2MnCl_4$, (b) $(C_6H_8N)_2MnBr_4$ and (c) $(C_6H_8N)_2MnI_4$ at different dose rates.

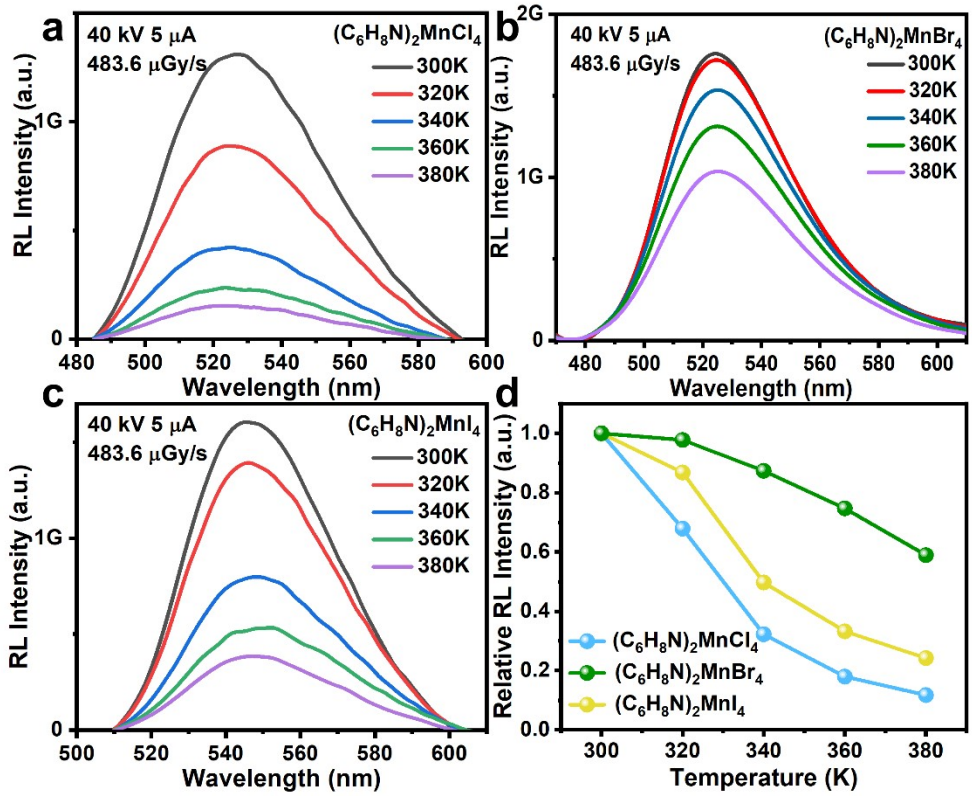

Fig. S13. Temperature-independent RL spectrum of (a) $(C_6H_8N)_2MnCl_4$, (b) $(C_6H_8N)_2MnBr_4$ and (c) $(C_6H_8N)_2MnI_4$. (d) Temperature-independent RL spectrum intensity of $(C_6H_8N)_2MnX_4$ (X=Cl, Br, I) and standard BGO scintillators.

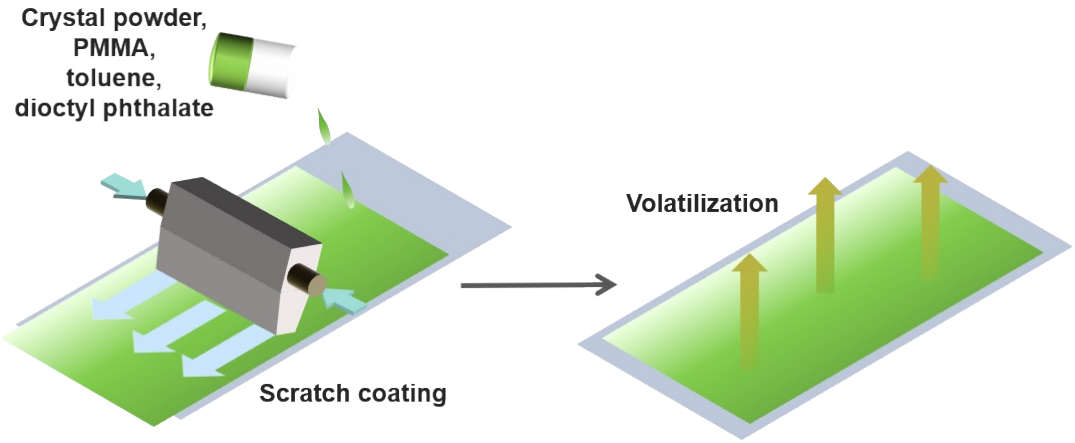

Fig. S14. Schematic diagram of preparing $(C_6H_8N)_2MnBr_4$ scintillator film.

Fig. S15. Thickness of $(C_6H_8N)_2MnBr_4$@PMMA film.

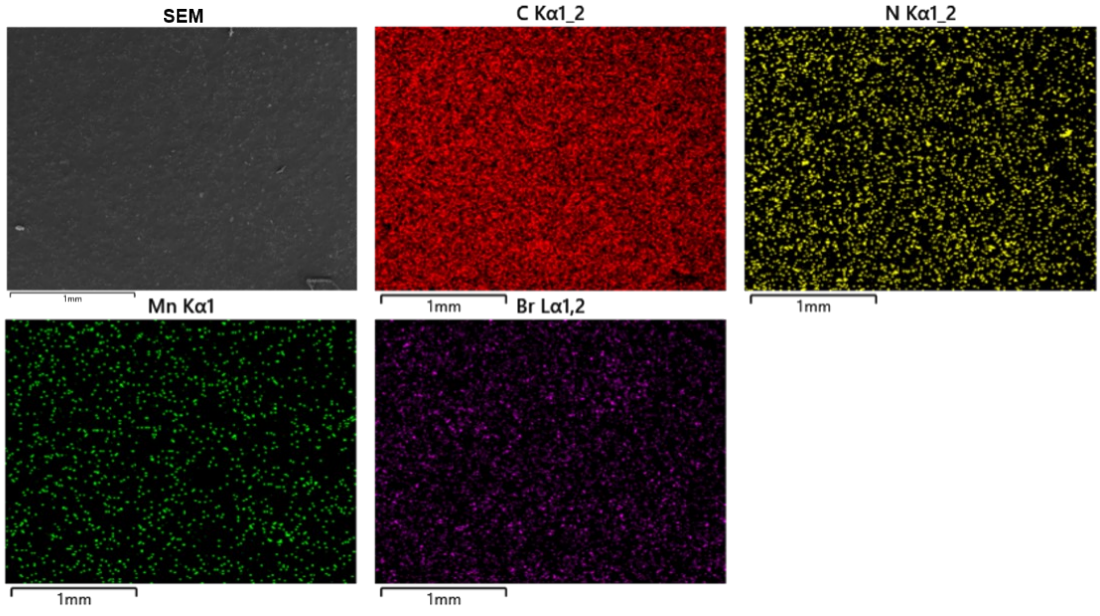

Fig. S16. Scanning electron microscopy (SEM) image and Energy-dispersive spectroscopy (EDS) elemental mapping images of C, N, Mn and Br of $(C_6H_8N)_2MnBr_4$@PMMA film.

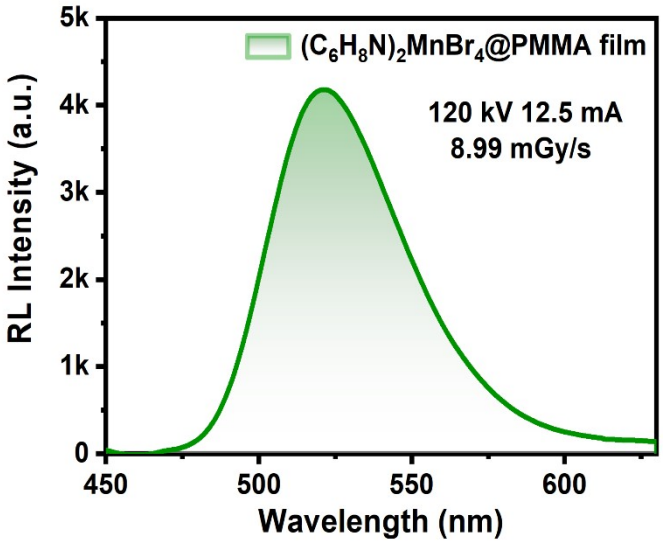

Fig. S17. The RL spectrum of $(C_6H_8N)_2MnBr_4$@PMMA film.

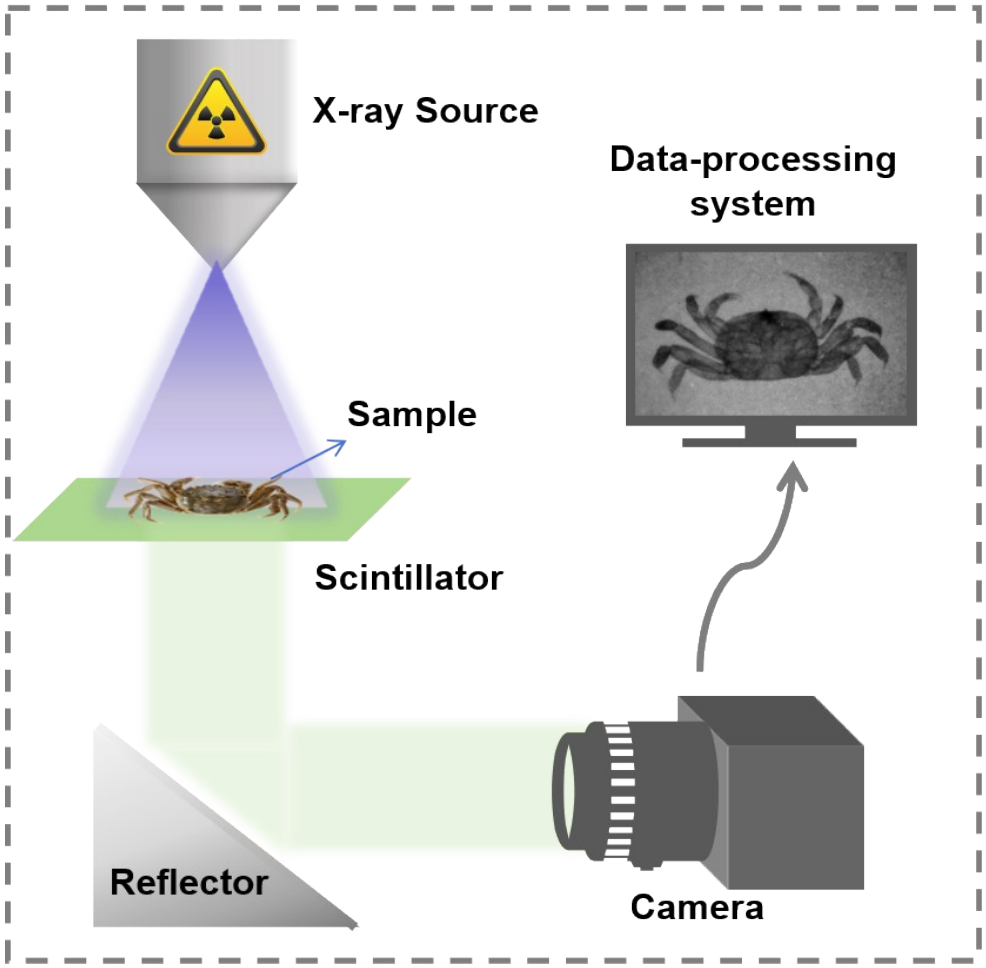

Fig. S18. Schematic diagram of our self-built X-ray imaging system.